Bond Stripe Patterns in SU (3) spin model on checkerboard lattice

Jun-Hao Zhang,[1,*] Jie Hou,[1] Jie Lou,[1,†] and Yan Chen[1,‡]

[1]*Department of Physics and State Key Laboratory of Surface Physics, Fudan University, Shanghai 200433, China*

(Dated: October 18, 2024)

We study SU (3) spin model on checkerboard lattice as a generalization of the SU (2) Heisenberg model on Kagomé lattice. This model inherits the point-connected $(N+1)$-site local structure, which leads to geometric frustration. The ground state of the system is obtained by DMRG algorithm. It prefers global bond stripe patterns at proper system sizes and boundary conditions. The direction and structure of the bond stripe patterns are sensitive to the system size and boundary conditions. We also calculated several correlation functions. They show faster decay behaviors than in same model on square lattice. The 3-sublattice antiferromagnetic order and valence cluster solid order are suppressed. The stripes are raletively decoupled and can be rebuilt in quasi-one dimensional ladders. This signifies that frustration brings the SU (3) spin model in 2 dimensional lattice from the valence bond solid state towards the stripe state and even the spin-liquid phase.

I. INTRODUCTION

Frustrated magnets have attracted a lot of research interest in the last decades. With the regular magnet orders being suppressed, quantum fluctuations play a dominant role in the low-energy physics of frustrated magnets. Various complex quantum effects including quantum criticality, topological orders, and long range entanglement emerges in frustrated magnets. Exotic quantum phases such as quantum spin liquid have been discovered in frustrated spin systems. In the model studies, the frustrated magnets will exhibit rich properties depending on the source of frustration of the system and the characteristics of the system.

A kind of the interesting systems are those with SU (N) symmetry. It can be realized with alkaline-earth-like atoms (such as ^{179}Yb and ^{87}Sr) trapped in an optical lattice, whose valence electrons in the outermost shell don't show magnetism externally[1–4]. Instead, the interactions of the hyperfine structure can be manipulated finely by orbital Feshbach resonance [5–7] that the systems hold SU (N) symmetry [8, 9]. Various geometrys of optical lattices and different values of N is realized and studied experimentally [10–14]. Recently, some new cooling methods are developed for quantum simulations of two-dimensional systems of Hubbard or Heisenberg type [15, 16].

These system are often decribed as SU (N) Fermi Hubbard models [17]. It is a natural generalisation of the conventional Fermi Hubbard model, with hoping parameter t and on-site repulsion U. This model has been intensively studied in the last decades [18–21]. Recent research on square research for $N = 3$ show metal-insulator transition and quantum antiferromagnetic order of different period near integer fillings [22, 23]. For one-dimensional system, trion molecular superfluid order and topological phases are discovered [24, 25]. As the strong correlated limit of SU (N) Fermi Hubbard model, SU (N) t-J model also have unique properties [26–28]

The spin model we interest in this paper is occurs at $1/N$-filling ($\langle n\rangle = 1$) in large U limit for the SU (N) Fermi Hubbard model [29]. At this point, charge fluctuations are suppressed by Mott physics and the interaction between spin degree of freedom can be calculated by 2nd order pertubation theory.

The research to SU (N) spin models in 2 dimensional systems discovered numerous novel physics [30, 31]. Large N approxiamtion meanfield calculation gives a general picture of the SU (N) Heisenberg model [21, 29, 32, 33]. The phase diagram include chiral spin liquid for large N, valence cluster solid for small N and some stripe state with flux for medium N. The chiral spin liquid phase is also confirmed in tensor network calculation of some SU (N) spin model with chiral interaction [34–36] For the case of $N = 3$, three-sublattice order are predicted from multiple method for square lattice [37–40]. On the other hand, there are also DMRG results showing it to be an fragile nematic spin liquid [41, 42]. Taking the advantage of this non-abelian symmetry, many state-of-the-art numerical technique are also developed for these system and get results with incredible scale and precision [43, 44].

For SU (N) spin model, the local frustrated structure is different from the SU (2) case. The local frustration structure changes from a triangular to a tetrahedron. The checkerboard lattice discussed in this paper is not only a 2D combination of local frustrated structures sharing corners, but also a kind of line graph lattice. The line graph lattice are the link-point duality of the original lattice, same as Kagomé lattice. They have a great degenaracy in energy spectrum for tight-binding model, leading to a flat energy band. This feature bring many interesting physics such as nontrivial topology, band ferromagnetism [45–50]. Experimentally, this lattice has been realized in monolayer Cu_2N [51]. The conventional spin model on checkerboard lattice has recieved significant attention from theorists [52–59]. This lattice is also studied for the SU (4) spin model as an appropriate system for 4-site simplex VCS state [60].

In this paper, we study the ground state of the frustrated SU (3) spin model on checkerboard lattice. We calculate ground state for a Hamiltonian tuned from square lattice to checkerboard lattice by ED and DMRG calculations. We observe a quantum phase transition between the models by both algorithms. For ED result, the degenracy of ground state

* jhzhang16@fudan.edu.cn
† loujie@fudan.edu.cn
‡ yanchen99@fudan.edu.cn;

changes, and the correlation become weaker in DMRG result. We also compare various low energy states calcualted by DMRG and identify from the results that a bond stripe pattern is favorable in terms of energy. Then we study the nature of stripe states and find that the bond stripes are almost decoupled. Thus, we characterize the single stripe and reproduce the stripe in quasi-one-dimensional ladders. Finally, we summarize our results and discuss the relation to the previous works and some low energy effective theory.

The organization of our paper is as follows. In Sec. II, we introduce the SU (3) Heisenberg model on chechkerboard lattice and the parameter settings of the DMRG simulations. In Sec. III, we show our numerical results including the various correlations and different local quantities. In Sec. IV, we study the nature of stripe states and reproduce the stripe in quasi-one-dimensional ladders The final section Sec. V is the summary and discussion.

II. MODEL

A. SU (3) symmetric Hamiltonian

The 2-site SU (3) symmetric spin Hamiltonian is constructed by taking $N = 3$ with general SU (N) Heisenberg exchange Hamiltonian

$$\mathcal{H}_{ij}^{\mathrm{SU}(N)} = JP_{ij} = JS_i^{\alpha\beta}S_j^{\beta\alpha}, \tag{1}$$

where P_{ij} exchanges local state on 2 sites, and $S_i^{\alpha\beta} = c_{i\alpha}^{\dagger}c_{i\beta}$ are the SU (N) spin operators in terms of fermion operators. The summations of α and β go over the N flavors of spin. In the following we will concentrate on the case with fundamental irrep described by Young diagram □. There are several good quantum number for this interaction. The total spin components $L^{3,8}$ together with 2nd Casimir C^2 are conserved. The numerical calculation can be accelerated by taking advantage of these good quantum numbers.

B. Checkerboard Lattice

The geometric frustration for ordinary spin system is often illustrated by triangle structures [61, 62]. For local irrep forming singlet by 2 sites, such as SU (2) spin system, model on Kagomé lattice are researched as frustrated magnets. It consists of triangles sharing only 1 corner with each of their neighbors. Singlet formation for SU (3) symmetry require 3 fundamental irreps. Specifically, singlet would occupy 3 sites in Hamiltonian Eq. (1). Therefore, the local frustration structure should be generalized to connected 4 sites(FIG. 1). By repeating this structure sharing only 1 corner with each of their neighbors, we can get pyrochlore lattice in 3D. Checkerboard lattice is alternative choice as the planar pyrochlore structure(FIG. 1). These lattices can be classified as line graphs of different original lattices with a flat upper energy band.

To relate with the previous results for square lattice, checkerboard lattice is regarded as a square lattice with next-nearest-neighbor interactions on half of the plaquette. The Hamiltonian could be written as

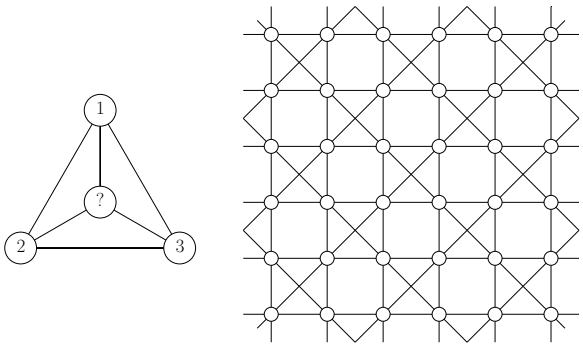

FIG. 1: Local frustration structure for SU (3) fundamental irreps (left panel) and checkerboard lattice (right panel).

$$H_{\text{Checkerboard}}^{\mathrm{SU}(N)} = \sum_{\langle i,j\rangle} JS_i^{\alpha\beta}S_j^{\beta\alpha} + \sum_{\langle\langle i,j\rangle\rangle}^{\text{half plaquette}} J_{\times}S_i^{\alpha\beta}S_j^{\beta\alpha}. \tag{2}$$

By taking $J_{\times}$ from 0 to J, we can tune the system from square lattice to checkerboard lattice. This would tell whether the ground states are in the same phase as ground state on square lattice. With no loss of generality, henceforth we choose $J \equiv 1$ to set the overall energy scale. The size of unit cells in checkerboard lattice is twice the ones in underlying square lattice, which contains 2 sites. The length of the base vector is $\sqrt{2}a$, and the direction is rotated $\pi/4$ relative to the square lattice.

III. NUMERICAL RESULTS

We use ED and DMRG to study the ground state of this model. For ED calculations, we use the QuSpin package [63, 64]. Periodic boundary condition is applied for both directions. Meanwhile the DMRG simulations is performed with the help of ITensor library [65]. A maximum bond dimension $D_{\text{max}} = 6000$ is kept in DMRG simulations. The calculation is typically performed for around 100 sweeps, and the largest truncation errors of final wave functions are about 10^{-5}. The global conversation of SU (3) spin component is kept as good quantum numbers for saving computing resources.

A. ED Result

We calculate the energy spectrum of several lowest energy state for the system with size 3×3 unit cells, which contains 18 sites. In order to identify different phases, the NNN interaction strength $J_{\times}$ varies from 0 to 1. The spectrum is illustrated in Fig. 2. A phase transition is found near $J_{\times} = 0.45$, where energy levels intersect. The ground state is unique for $J_{\times} < 0.45$ and 2-fold degenerate for $J_{\times} > 0.45$.

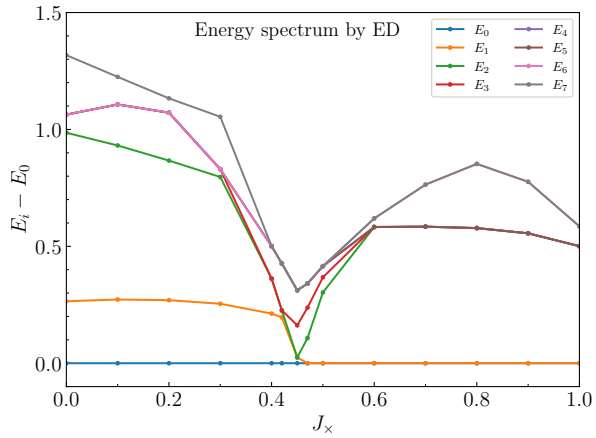

FIG. 2: Low energy spectrum of 3×3 system.

This 2-fold degenaracy could be splitted by breaking the lattice symmetry from c_4 to c_2. Specifically, we can apply different $J_\times$ on different direction to split 2-fold degenerate ground states. We obtain the coupling strength along interaction bonds, the 2 degenerate ground states shows slight difference in the NNN couplings along different directions. The local spin component n_i^α and coupling strength $B_{ij} = \hat{L}_i^3 \hat{L}_j^3$is shown in Fig. 3. The NNN coupling strengths along 2 directions are B_{NNN} have little difference in value as -0.104 and -0.093. Thus, the degenerate ground states are symmetry-breaking states, probably like nematic spin liquid [42]. Moreover, when $J_\times$ become stronger than 1.15, the ground state become direct product of 6 singlets along the x, y directions. The limited system size introduces singlet configuration cross the boundary, which is not allowed in thermodynamic limit.

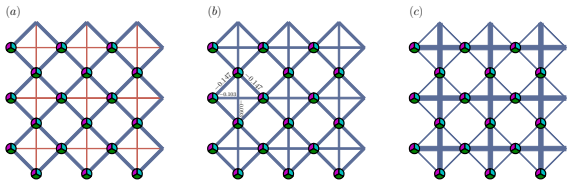

(a) $J_\times = 0.10$ (b) $J_\times = 0.90$ (c) $J_\times = 1.18$

FIG. 3: Real-space coupling patterns of the ground states in two phases. (a) unique ground state when $J_\times = 0.10$; (b) one of two degenerate ground states when $J_\times = 0.90$; (c) unique ground state when $J_\times = 1.18$. The pie charts represent the local spin component on each site. The width of lines represents the strength of coupling. Its color takes blue and red for antiferromagnetic and ferromagnetic coupling.

B. DMRG Result

The ED result shows a phase transition between square and planar pyrochlore lattice. However it introduces strong finite size effects and provides little information about correlations. Then we study the ground state with DMRG algorithm for larger system size.

The DMRG calculation are performed on cylinders, with open boundary conditions in x direction and periodic boundary conditions in y direction. The system size is set as $N_x \times N_y$ unit cells, including $N_{\text{tot}} = 2N_xN_y + N_y$ sites. The extra N_y sites are boundary sites on one of the open boundaries. We calculate several different sizes, with N_x varies from 7 to 10, and N_y varing from 4 to 6. The size of the systems are chosen such that N_{tot} is a multiple of 3.

Corresponding to the results of ED, we study the evolution of the ground state as $J_\times$ from 0 to 1. We measure the spin correlation function

$$S(r) = \left\langle \hat{L}_i^3 \hat{L}_{i+\vec{r}}^3 \right\rangle, \tag{3}$$

where $\hat{L}_i^3 = \hat{n}_i^{\alpha=1} - \hat{n}_i^{\alpha=2}$ is one of the Gell-Man generator. Different behaviors are observed for weak and strong NNN interactions(Fig. 4a). It shows a shorter correlation length in the strong interaction case, significantly different from weak interaction cases. This indicates a phase transition between ground states on square and planar pyrochlore lattice.

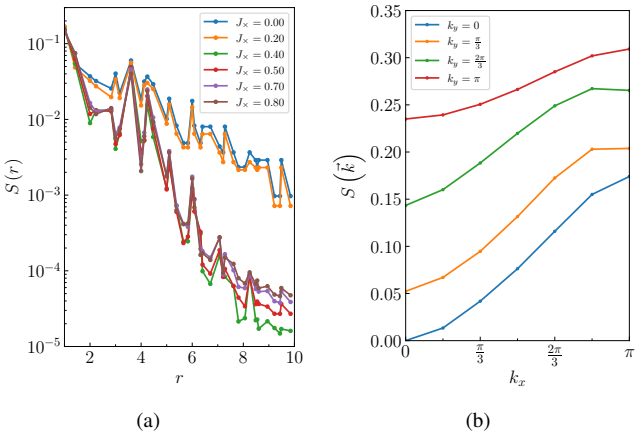

(a) (b)

FIG. 4: Spin correlation (a) Spin correlation with different $J_\times$; (b) Fourier transform of spin correlation.

The shorter spin correlation length indicates the break of 3-sublattice antiferromagnetic order. The fourier transformation of the spin correlation function is shown in Fig. 4b. It is smooth and has a underlying quadratic behaviors near the origin, meaning that there is no spin order and probably finite spin gap. We also study planar pyrochlore lattice systems in square lattice geometry (Details in Supplemental Materials). The spin correlation function along the side of the plaquette shows a short correlation length of $r_S = 0.91a$. We also try to induce 3-sublattice AF order and valence bond / cluster solid order by applying corresponding field on the boundary. The results don't support these orders. (Details in Supplemental Materials)

C. Real-Space Valence Bond Coupling

After confirming the absence of 3-sublattice antiferromagnetic order and simple triangular VCS order, we focus lattices on unit cell direction. The ground states exhibit some real space structure in varies of system sizes. In the system size $(7, 4)$ (no long singlet cross the boundary, 60 sites in total as multiple of 3), the local valence bond strength of the lowest energy state shows a stripe pattern (Fig. 5a). This stripe pattern has a period of 3 unit cell lengths in the x direction, and don't break translational symmetry in the y direction. Sometimes the DMRG simulation would converge to another ground state structure. It has a apparent local triangle pattern in valence bond strength, but the triangles are not arranged in a clear periodicity as a VCS phase. The energy of this local minimum state is also a little higher than the stripe pattern state.

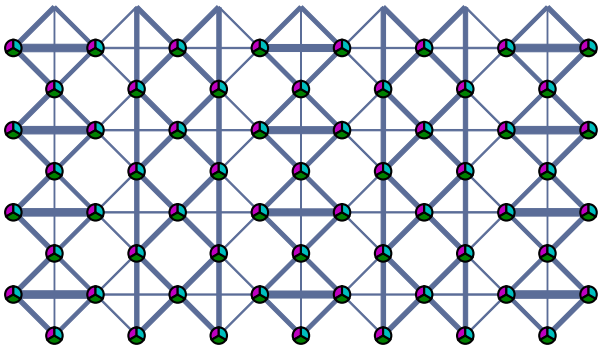

(a) $(7, 4)$ Stripe Structure

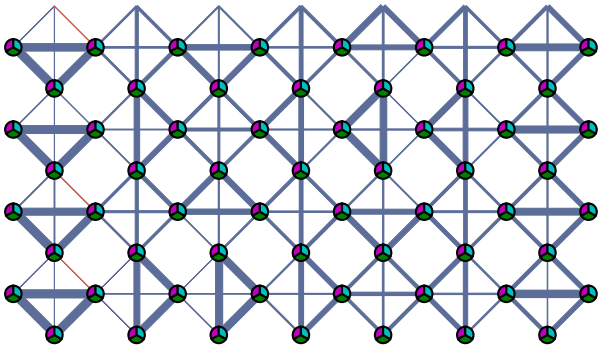

(b) $(7, 4)$ Local Minimum

FIG. 5: (5a) Ground state and (5b) local minimum state real-space bond strength obtained by DMRG simulation for the system size of $(7, 4)$. The energy of the states are (5a) $E_0 = -201.698$, (5b) $E_1 = -201.468$.

We also calculate the ground state of larger system sizes, up to $(10, 6)$ (Details in Supplemental Materials). There are local minimum states for different system sizes. We summarize some of the lowest energy states for differnent sizes in Table I.

We discover several coupling laws for this model. The coupling structure near system boundary has significant features. For the staight open boundaries longer than 5 unit cells, the coupling structure is arranged by repeated triangles, which breaks reflection symmetry along the boundary. For 4 unit cell width case, the reflection symmetric boundary could be regarded as superposition of triangle arraies with different orientations. The stronger coupling strength on the bond vertical to the boundary These triangular singlets are connected into a boundary ring. Reflection transformation to this boundary ring would not change system energy.

For systems with length $3n + 1$ in x direction, the stripe phase with 3-unti-cell stripe has better energy. This stripe pattern is consist of a one-unit-cell-width triangle array as boundary pattern and a 2-unit-cell-width reflecting symmetric pattern. We call the strong coupling bond as a flat stripe. The energy of the flat stripe is lower than the energy of two corresponding staggered triangle VCS patterns. By compare local minimum states in same size, we find the more stripe pattern the better energy it has.

For systems with other lengths in x direction, the stripe phase can't fit the system well. When the length in y direction is 6, there is a clear triangle pattern. It shows a 2-unit-cell-width periodic triangle configuration away from the open boundary. As the length in x direction increases, this triangle configuration would make up a vertical stripe-like configuration. So we come to the domain law that stripe pattern reduce the local energy, while the boundary pattern serves as a constraint to the global coupling structure.

For stripe phase, we calculate several correlation functions and show them in Fig. 6. It includes spin correlation function Eq. (3), chiral correlation function

$$\chi(r) = \langle \chi_{ijk} \chi_{i'j'k'} \rangle , \tag{4}$$

and nematic correlation function

$$\eta(r) = \langle \eta_x \eta_{x+r} \rangle - \langle \eta_x \rangle \langle \eta_{x+r} \rangle . \tag{5}$$

The local chiral and nematic operators are defined as $\chi_{ijk} = i\left(P_{ijk} - P_{ijk}^{-1}\right)$ and $\eta_{\mathrm{i}} = (B_{\mathrm{i}}^{x} - B_{\mathrm{i}}^{y})$, where P_{ijk} rotate states on 3 sites and $B_i^{x,y}$ is bond coupling along the x, y in a unit cell. These correlation functions show exponential decay, with short correlation range less than the length of the square side. This result excludes the possibility of these orders in checkerboard lattice.

IV. BOND STRIPE PATTERN

Bond stripe patterns have been discovered in meanfield calculation for SU (N) Heisenberg model by self-consistent minimization algorithm. They are low energy states for $N = 4, 5$ on triangle lattice and $N = 5, 6$ on square and J_1-J_2 honeycomb lattice [32, 33, 66]. Nevertheless, the bond stripe state they find is doubled unit-cell one, in significantly contrast to the tripled unit-cell stripe phase in this work. The stripe states they discover have $U(1)$ guage flux which is not found in the bond stripe state. On the other hand, the ground state for

Algorithm	Size	Number of Spins	Number of bonds	Valence Bond Coupling Structure	Energy	Energy per bond
ED	$(3,3)$	18	54	Nematic(Fig. 3b)	-64.343	-1.1915
DMRG	$(7,4)$	60	168	Triangle(Fig. 5b)	-201.468	-1.1992
				Stripe(Fig. 5a)	-201.698	-1.2006
	$(10,4)$	84	240	Stripe(Fig. S2a)	-286.548	-1.1940
				Triangle & Stripe(Fig. S2b)	-286.283	-1.1928
	$(7,5)$	75	210	Incompatible(Fig. S3b)	-250.520	-1.1929
				Stripe(Fig. S3a)	-250.928	-1.1949
	$(7,6)$	90	252	Incompatible(Fig. S3d)	-299.661	-1.1891
				Stripe(Fig. S3c)	-300.598	-1.1928
	$(8,6)$	102	288	Triangle(Fig. S4a)	-342.361	-1.1887
	$(9,6)$	114	324	Incompatible(Fig. S4b)	-384.193	-1.1858
				Triangle(Fig. S4d)	-384.070	-1.1854
				Triangle & Stripe(Fig. S4c)	-384.550	-1.1868
	$(10,6)$	126	360	Triangle(Fig. S4e)	-426.819	-1.1856
				Stripe(Fig. S4f)	-426.903	-1.1858

TABLE I: Energy of the ground state and local minimum states for different system sizes.

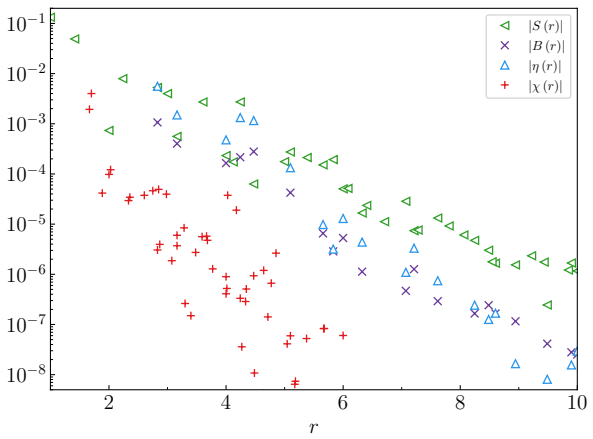

FIG. 6: Spin correlation $S(r)$, bond correlation $B(r)$, nematic correlation $\eta(r)$ and chiral correlation $\chi(r)$ measured in system with size $(N_x, N_y) = (10, 6)$. They all show exponential decay. The correlation lengths are $r_S = 0.89a$, $r_B = 0.55a$, $r_\eta = 0.61a$ and $r_\chi = 0.32a$, a is the length of square side.

$N = 3$ is VCS state which is consist of singlets with 3 or 6 sites in such mean-field calculations. The J_2 interaction suppresses the global VCS order and 3-sublattice order, making a bond stripe phase distinct from mean-field result.

The flat part of the stripe pattern would break translation symmetry in to triangle VCS pattern when meeting boundary triangle array or stripe corner. This implys the state is a direct product state. We calculate the entanglement entropy at different position of the division line in FIG. 7. The length dependence of entanglement entropy between the stripes is also calculated. The entanglement entropy for subsystems cutting weak bond is lowest and approximately equal for different boundary length of subsystems. We also infer from the periodicity of entanglement entropy that the range of entanglement is short. The stripes are seperated spin singlet on the occupied sites. This explains the range of correlation cross the stripes are necessarily short.

A. Decoupled Stripe and Single Stripe Ladder

Given that each stripe is a near pure state, the correlation in stripe could be calculated effectively on the ladder stripe occupying. We rebuild the single stripe patterns by ED in small system with 4-6 unit cells.

For triangle array, we get similar results to the previous exact solution of the spin tetrahedron chain [55]. The ground state is of two-fold degeneracy that could be break by violating the reflection symmetry. The symmetry broken states have same pattern as triangle array in stripe state. They are pure direct product states.

The flat stripe is also reproduced in isolated ladder system. The ground state is unique and have uniform coupling strength on each bond, $B = -0.1986$.

We further use DMRG algorithm to study the more long-range correlation functions within the stripes. The real space pattern is shown in FIG. 8a. The result for triangle array stripe ladder is consistent with the results of the ED calculation as a direct product of triangle singlets, whose correlation functions is consistent with the VCS state.

For the flat stripe ladder system, We compute the system length up to 64 unit cells, whose maximum kept dimension for truncation errors less than 10^{-10} is $D = 1467$. This limited dimensions suggests that this quasi-one-dimensional system is gapped. As what is shown in FIG. 8b, there is no spontaneous breaking of translational symmetry and spatial inver-

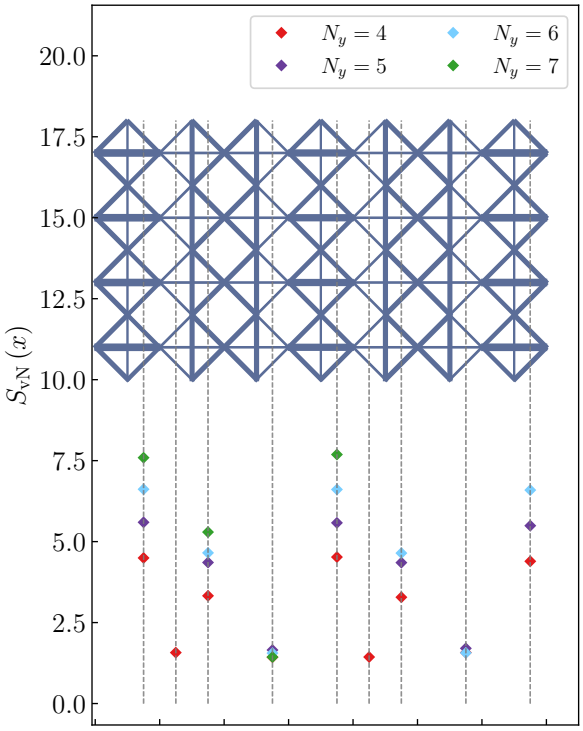

FIG. 7: Entanglement entropy for division at different position. The dashed lines mark the system division position and the red bars below represent the value of entanglement entropy at dashed line. It shows distinct periodicity, with approximate minima between stripes and maxima on cutting triangle arraies.

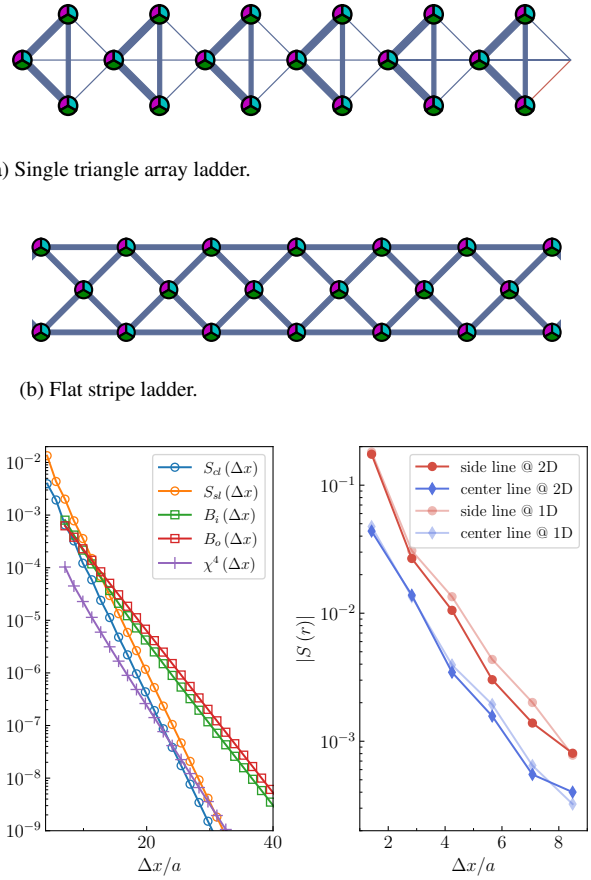

(a) Single triangle array ladder.

(b) Flat stripe ladder.

(c) Correlation function in flat stripe ladder.

FIG. 8: (a),(b) the local spin and bond pattern of the triangle array ladder and the flat stripe ladder, respectively. (c) (left) Spin correlation along center line S_{cl} and side line S_{sl}. Bond correlation of inner bonds B_i and outer bonds B_o. (right) Comparison of spin correlation functions for flat stripe in 2D and 1D system.

sion symmetry in the results of the DMRG calculations. When we examine the valence bond strengths away from the boundary, there is a difference between the valence bond strengths in the direction parallel to the chain direction and diagonal to the chain direction of $B_{=} = -0.1848$ and $B_{\times} = -0.1993$, respectively. This is similar to results for the two-dimensional case in the ratio (~ 0.93) of the two kinds of bonds (e.g. $B_{=}^{2d} = -0.175$ and $B_{\times}^{2d} = -0.1846$ in $(10, 6)$ system).

The correlation functions of the flat stripe ladder system also have highly similar behaviour to the 2-dimensional case. The spin and bond correlation functions for the flat stripe ladder system are shown in FIG. 8c . They both show exponential decay with correlation length $r_S^{1d} = 1.73a$ and $r_B^{1d} = 2.82a$ respectively. We caluclate the corresponding correlation function of 4-point chirality

$$\chi_{ijkl}^4 = \frac{i}{4}\left(P_{ijkl} - P_{ijkl}^{-1}\right), \tag{6}$$

where $ijkl$ is defined on the square part. They also decay exponentially, failing to corroborate the gauge flux of stripe state in mean-field calculations.

V. SUMMARY AND DISCUSSION

Singlet occupying 3 sites is frustrated on vertex-connected tetrahedrons, which form pyrochlore lattice. By using ED and DMRG simulations, we have studied the SU(3) spin model on checkerboard lattice cylinder, so-called the planar pyrochlore. We observe the quantum phase transition between the square lattice model and the checkerboard lattice model by tuning the diagonal couplings. The 3-sublattice antiferromagnetic order is suppressed when the diagonal couplings are added to the model. The stripe pattern appears frequently in the DMRG calculations, and the stripe state serve as global ground state in suitable system sizes. The 2-fold degenaracy of the ground states in ED calculation is also consistent with the c_4 symmetry breaking of stripe phase. The stripes are raletively decoupled, leading to short-ranged correlation functions in this phase. The stripe patterns consist of a triangle array stripe and a uniform flat stripe. They can be reproduced respectively in

the ladder model defined on the sites they occupy, in which the correlation in the stripe is short-ranged.

In previous meanfield studies of SU(3) spin model on various lattices [32, 33], the lowest energy state is VCS. The stripe and chiral spin liquid phase is discovered for larger N. The VCS-stripe mixing state discovered here can be regarded as a step closer to the chiral spin liquid phase accordng to general phase diagram results [32, 66, 67]. Whether extra interaction can induct spin liquid need further investigation.

Furthermore, under the 0th order approximation, the ground state of the model is degenarate patterns with local singlets on 3 of the vertices of one planar tetrahedron. The different triangle patterns expand a configuration space (Details in Supplemental Materials). Following the quantum dimer model study on Kagomé lattice [68], an arrow representaion could be build. Each site belongs to 1 singlet and shared by 2 tetrahedrons, so we could define the arrow on one site pointing to the the tetrahedron which singlet belongs to. This arrow representation forms a restricted vertex model, whose mechanism may be related to the $\mathbb{Z}_2$ gauge theory[69].

VI. ACKNOWLEDGMENTS

This work was supported by the National Key Research and Development Program of China Grant No. 2022YFA1404204 and the National Natural Science Foundation of China (Grants No. 11625416 and No. 12274086). The authors acknowledge Fudan High Performance Computation Center for providing HPC resources that have contributed to the numerical results reported in this paper.

[1] S. Stellmer, R. Grimm, and F. Schreck, Detection and manipulation of nuclear spin states in fermionic strontium, Phys. Rev. A **84**, 043611 (2011).
[2] S. Stellmer, M. K. Tey, B. Huang, R. Grimm, and F. Schreck, Bose-Einstein Condensation of Strontium, Phys. Rev. Lett. **103**, 200401 (2009).
[3] Y. N. M. de Escobar, P. G. Mickelson, M. Yan, B. J. DeSalvo, S. B. Nagel, and T. C. Killian, Bose-Einstein Condensation of ^{88}Sr, Phys. Rev. Lett. **103**, 200402 (2009).
[4] M. Kitagawa, K. Enomoto, K. Kasa, Y. Takahashi, R. Ciuryło, P. Naidon, and P. S. Julienne, Two-color photoassociation spectroscopy of ytterbium atoms and the precise determinations of s-wave scattering lengths, Phys. Rev. A **77**, 012719 (2008).
[5] M. Höfer, L. Riegger, F. Scazza, C. Hofrichter, D. Fernandes, M. Parish, J. Levinsen, I. Bloch, and S. Fölling, Observation of an Orbital Interaction-Induced Feshbach Resonance in ^{173}Yb, Phys. Rev. Lett. **115**, 265302 (2015).
[6] G. Pagano, M. Mancini, G. Cappellini, L. Livi, C. Sias, J. Catani, M. Inguscio, and L. Fallani, Strongly Interacting Gas of Two-Electron Fermions at an Orbital Feshbach Resonance, Phys. Rev. Lett. **115**, 265301 (2015).
[7] R. Zhang, Y. Cheng, H. Zhai, and P. Zhang, Orbital Feshbach Resonance in Alkali-Earth Atoms, Phys. Rev. Lett. **115**, 135301 (2015).
[8] M. A. Cazalilla, A. F. Ho, and M. Ueda, Ultracold gases of ytterbium: ferromagnetism and Mott states in an SU(6) Fermi system, New J. Phys. **11**, 103033 (2009).
[9] A. V. Gorshkov, M. Hermele, V. Gurarie, C. Xu, P. S. Julienne, J. Ye, P. Zoller, E. Demler, M. D. Lukin, and A. M. Rey, Two-orbital SU(N) magnetism with ultracold alkaline-earth atoms, Nat. Phys. **6**, 289 (2010).
[10] S. Taie, R. Yamazaki, S. Sugawa, and Y. Takahashi, An SU(6) Mott insulator of an atomic Fermi gas realized by large-spin Pomeranchuk cooling, Nat. Phys. **8**, 825 (2012).
[11] C. Hofrichter, L. Riegger, F. Scazza, M. Höfer, D. R. Fernandes, I. Bloch, and S. Fölling, Direct probing of the mott crossover in the SU(N) Fermi-Hubbard model, Phys. Rev. X **6**, 021030 (2016).
[12] H. Ozawa, S. Taie, Y. Takasu, and Y. Takahashi, Antiferromagnetic Spin Correlation of SU (N) Fermi Gas in an Optical Superlattice, Phys. Rev. Lett. **121**, 225303 (2018).
[13] D. Tusi, L. Franchi, L. F. Livi, K. Baumann, D. Benedicto Orenes, L. Del Re, R. E. Barfknecht, T.-W. Zhou, M. Inguscio, G. Cappellini, M. Capone, J. Catani, and L. Fallani, Flavour-selective localization in interacting lattice fermions, Nat. Phys. **18**, 1201 (2022).
[14] S. Taie, E. Ibarra-García-Padilla, N. Nishizawa, Y. Takasu, Y. Kuno, H.-T. Wei, R. T. Scalettar, K. R. A. Hazzard, and Y. Takahashi, Observation of antiferromagnetic correlations in an ultracold SU(N) Hubbard model, Nat. Phys. **18**, 1356 (2022).
[15] A. M. Müller, M. Lajkó, F. Schreck, F. Mila, and J. Minář, State selective cooling of SU (N) Fermi gases, Phys. Rev. A **104**, 013304 (2021).
[16] D. Yamamoto and K. Morita, Engineering of a Low-Entropy Quantum Simulator for Strongly Correlated Electrons Using Cold Atoms with $\mathrm{SU}(\mathcal{N})$-Symmetric Interactions, Phys. Rev. Lett. **132**, 213401 (2024).
[17] C. Honerkamp and W. Hofstetter, Ultracold fermions and the SU(N) hubbard model, Phys. Rev. Lett. **92**, 170403 (2004).
[18] A. Sotnikov and W. Hofstetter, Magnetic ordering of three-component ultracold fermionic mixtures in optical lattices, Phys. Rev. A **89**, 063601 (2014).
[19] A. Sotnikov, Critical entropies and magnetic-phase-diagram analysis of ultracold three-component fermionic mixtures in optical lattices, Phys. Rev. A **92**, 023633 (2015).
[20] M. Hafez-Torbati and W. Hofstetter, Artificial SU(3) spin-orbit coupling and exotic Mott insulators, Phys. Rev. B **98**, 245131 (2018).
[21] G. Chen, K. R. Hazzard, A. M. Rey, and M. Hermele, Synthetic-gauge-field stabilization of the chiral-spin-liquid phase, Phys. Rev. A **93**, 245159 (2016).
[22] C. Feng, E. Ibarra-García-Padilla, K. R. A. Hazzard, R. Scalettar, S. Zhang, and E. Vitali, Metal-insulator transition and quantum magnetism in the SU(3) Fermi-Hubbard model, Phys. Rev. Res. **5**, 043267 (2023).
[23] E. Ibarra-García-Padilla, C. Feng, G. Pasqualetti, S. Fölling, R. T. Scalettar, E. Khatami, and K. R. A. Hazzard, Metal-insulator transition and magnetism of SU(3) fermions in the square lattice, Phys. Rev. A **108**, 053312 (2023).
[24] R. Assaraf, P. Azaria, M. Caffarel, and P. Lecheminant, Metal-insulator transition in the one-dimensional SU (N) Hubbard model, Phys. Rev. B **60**, 2299 (1999).

[25] S. Capponi, P. Lecheminant, and K. Totsuka, Phases of one-dimensional SU(N) cold atomic Fermi gases-From molecular Luttinger liquids to topological phases, Ann. Phys. (NY) **367**, 50 (2016).

[26] J.-C. He, J.-H. Zhang, J. Lou, and Y. Chen, Six-component pairing instability in the su(4) t-j chain (2023), arXiv:2311.06601.

[27] H. Schlömer, F. Grusdt, U. Schollwöck, K. R. A. Hazzard, and A. Bohrdt, Subdimensional magnetic polarons in the one-hole doped SU(3) $t-J$ model, Phys. Rev. B **110**, 125134 (2024).

[28] J. Zhang, J. Hou, J. Lou, and Y. Chen, Ground state phase diagram of SU(3) t-j chain (2024), arXiv:2409.09344.

[29] M. Hermele and V. Gurarie, Topological liquids and valence cluster states in two-dimensional SU(N) magnets, Phys. Rev. B **84**, 245159 (2011).

[30] A. Szasz, C. Wang, and Y.-C. He, Phase diagram of a bilinear-biquadratic spin-1 model on the triangular lattice from density matrix renormalization group simulations, Phys. Rev. B **106**, 115103 (2022).

[31] R. Kaneko, S. Goto, and I. Danshita, Ground-state phase diagram of the SU(4) Heisenberg model on a plaquette lattice, Phys. Rev. A **110**, 023326 (2024).

[32] X.-P. Yao, Y. Gao, and G. Chen, Topological chiral spin liquids and competing states in triangular lattice SU (N) Mott insulators, Phys. Rev. Res. **3**, 023138 (2021).

[33] X.-P. Yao, R. L. Luo, and G. Chen, Intertwining SU(N) symmetry and frustration on a honeycomb lattice, Phys. Rev. B **105**, 024401 (2022).

[34] J.-Y. Chen, J.-W. Li, P. Nataf, S. Capponi, M. Mambrini, K. Totsuka, H.-H. Tu, A. Weichselbaum, J. von Delft, and D. Poilblanc, Abelian $\mathrm{SU}(N)_1$ chiral spin liquids on the square lattice, Phys. Rev. B **104**, 235104 (2021).

[35] S. Niu, J.-W. Li, J.-Y. Chen, and D. Poilblanc, Chiral spin liquids with projected Gaussian fermionic entangled pair states, Phys. Rev. B **109**, L081107 (2024).

[36] Y. Xu, S. Capponi, J.-Y. Chen, L. Vanderstraeten, J. Hasik, A. H. Nevidomskyy, M. Mambrini, K. Penc, and D. Poilblanc, Phase diagram of the chiral SU(3) antiferromagnet on the kagome lattice, Phys. Rev. B **108**, 195153 (2023).

[37] T. A. Tóth, A. M. Läuchli, F. Mila, and K. Penc, Three-sublattice ordering of the SU(3) Heisenberg model of three-flavor fermions on the square and cubic lattices, Phys. Rev. Lett. **105**, 265301 (2010).

[38] B. Bauer, P. Corboz, A. M. Läuchli, L. Messio, K. Penc, M. Troyer, and F. Mila, Three-sublattice order in the SU(3) Heisenberg model on the square and triangular lattice, Phys. Rev. B **85**, 125116 (2012).

[39] A. Läuchli, F. Mila, and K. Penc, Quadrupolar Phases of the $S = 1$ Bilinear-Biquadratic Heisenberg Model on the Triangular Lattice, Phys. Rev. Lett. **97**, 087205 (2006).

[40] A. Läuchli, F. Mila, and K. Penc, Erratum: Quadrupolar Phases of the $S = 1$ Bilinear-Biquadratic Heisenberg Model on the Triangular Lattice [Phys. Rev. Lett. 97, 087205 (2006)], Phys. Rev. Lett. **97**, 229901 (2006).

[41] W.-J. Hu, S.-S. Gong, H.-H. Lai, Q. Si, and E. Dagotto, Density matrix renormalization group study of nematicity in two dimensions: Application to a spin-1 bilinear-biquadratic model on the square lattice, Phys. Rev. B **101**, 014421 (2020).

[42] X.-T. Zhang, W.-J. Hu, E. Dagotto, and S. Gong, Fragility of the nematic spin liquid induced by diagonal couplings in the square-lattice SU(3) model, Phys. Rev. B **104**, 195135 (2021).

[43] T. Botzung and P. Nataf, Exact Diagonalization of $\mathrm{SU}(N)$ Fermi-Hubbard Models, Phys. Rev. Lett. **132**, 153001 (2024).

[44] A. Weichselbaum, Qspace-an open-source tensor library for abelian and non-abelian symmetries, arXiv:2405.06632 10.48550/arXiv.2405.06632 (2024).

[45] K. Sun, Z. Gu, H. Katsura, and S. Das Sarma, Nearly Flatbands with Nontrivial Topology, Phys. Rev. Lett. **106**, 236803 (2011).

[46] T. Yoshioka, A. Koga, and N. Kawakami, Frustration effects in an anisotropic checkerboard lattice Hubbard model, Phys. Rev. B **78**, 165113 (2008).

[47] S. Fujimoto, Geometrical-Frustration-Induced (Semi)Metal-to-Insulator Transition, Phys. Rev. Lett. **89**, 226402 (2002).

[48] H. Katsura and A. Tanaka, Nagaoka states in the SU(n) Hubbard model, Phys. Rev. A **87**, 013617 (2013).

[49] K. Tamura and H. Katsura, Ferromagnetism in the SU(n) Hubbard model with a nearly flat band, Phys. Rev. B **100**, 214423 (2019).

[50] K. Tamura and H. Katsura, Ferromagnetism in d-Dimensional SU(n) Hubbard Models with Nearly Flat Bands, J. Stat. Phys. **182**, 16 (2021).

[51] X. Hu, R.-W. Zhang, D.-S. Ma, Z. Cai, D. Geng, Z. Sun, Q. Zhao, J. Gao, P. Cheng, L. Chen, K. Wu, Y. Yao, and B. Feng, Realization of a Two-Dimensional Checkerboard Lattice in Monolayer $\mathrm{Cu_2N}$, Nano Lett. **23**, 5610 (2023).

[52] B. Canals, From the square lattice to the checkerboard lattice: Spin-wave and large-n limit analysis, Phys. Rev. B **65**, 184408 (2002).

[53] J.-B. Fouet, M. Mambrini, P. Sindzingre, and C. Lhuillier, Planar pyrochlore: A valence-bond crystal, Phys. Rev. B **67**, 054411 (2003).

[54] J.-S. Bernier, C.-H. Chung, Y. B. Kim, and S. Sachdev, Planar pyrochlore antiferromagnet: A large-N analysis, Phys. Rev. B **69**, 214427 (2004).

[55] S. Chen, Y. Wang, W. Q. Ning, C. Wu, and H. Q. Lin, Exact ground state and elementary excitations of the spin tetrahedron chain, Phys. Rev. B **74**, 174424 (2006).

[56] O. A. Starykh, A. Furusaki, and L. Balents, Anisotropic pyrochlores and the global phase diagram of the checkerboard antiferromagnet, Phys. Rev. B **72**, 094416 (2005).

[57] R. F. Bishop, P. H. Y. Li, D. J. J. Farnell, J. Richter, and C. E. Campbell, Frustrated Heisenberg antiferromagnet on the checkerboard lattice: J_1-J_2 model, Phys. Rev. B **85**, 205122 (2012).

[58] P. H. Y. Li and R. F. Bishop, Ground-state phase structure of the spin- anisotropic planar pyrochlore, J. Phys.: Condens. Matter **27**, 386002 (2015).

[59] S. Capponi, Numerical study of magnetization plateaus in the spin-$\frac{1}{2}$ Heisenberg antiferromagnet on the checkerboard lattice, Phys. Rev. B **95**, 014420 (2017).

[60] P. Corboz, K. Penc, F. Mila, and A. M. Läuchli, Simplex solids in SU(N) Heisenberg models on the kagome and checkerboard lattices, Phys. Rev. B **86**, 041106 (2012).

[61] L. Balents, Spin liquids in frustrated magnets, Nature **464**, 199 (2010).

[62] C. Lacroix, P. Mendels, and F. Mila, eds., *Introduction to Frustrated Magnetism: Materials, Experiments, Theory*, Springer Series in Solid-State Sciences, Vol. 164 (Springer, 2011).

[63] P. Weinberg and M. Bukov, QuSpin: a Python package for dynamics and exact diagonalisation of quantum many body systems part I: spin chains, SciPost Phys. **2**, 003 (2017).

[64] P. Weinberg and M. Bukov, QuSpin: a Python package for dynamics and exact diagonalisation of quantum many body systems. Part II: bosons, fermions and higher spins, SciPost Phys. **7**, 020 (2019).

[65] M. Fishman, S. R. White, and E. M. Stoudenmire, The ITensor Software Library for Tensor Network Calculations, SciPost Phys. Codebases , 4 (2022).

[66] M. Hermele, V. Gurarie, and A. M. Rey, Mott Insulators of Ultracold Fermionic Alkaline Earth Atoms: Underconstrained Magnetism and Chiral Spin Liquid, Phys. Rev. Lett. **103**, 135301 (2009).
[67] C. Boos, C. J. Ganahl, M. Lajkó, P. Nataf, A. M. Läuchli, K. Penc, K. P. Schmidt, and F. Mila, Time-reversal symmetry breaking Abelian chiral spin liquid in Mott phases of three-component fermions on the triangular lattice, Phys. Rev. Res. **2**, 023098 (2020).
[68] G. Misguich, D. Serban, and V. Pasquier, Quantum Dimer Model on the Kagome Lattice: Solvable Dimer-Liquid and Ising Gauge Theory, Phys. Rev. Lett. **89**, 137202 (2002).
[69] H. Yan and R. Pohle, Classical $\mathbb{Z}_2$ spin liquid on the generalized four-color kitaev model (2024), arXiv:2409.04061.

Supplemental Materials for "Bond Stripe Patterns in $\mathrm{SU}(3)$ spin model on checkerboard lattice"

S1. DMRG SIMULATION IN SQUARE FRAME

The interaction we tune turns the lattice from a square one to a planar pyrochlore. The ground state pattern in square frame direction are calculated as a reference to verify the existence of the possible order. 3-sublattice antiferromagnetic order are obviously suppressed from the very short penetration depth of the spin polarisation (FIG. S1(a)). We also try to induce valence bond order by some stronger interaction near boundary (FIG. S1$(b)-(d)$). The inhomogeneity of bond just extend to as far as several unitcells, with staggered bonds induced by open boundary on x direction remaining.

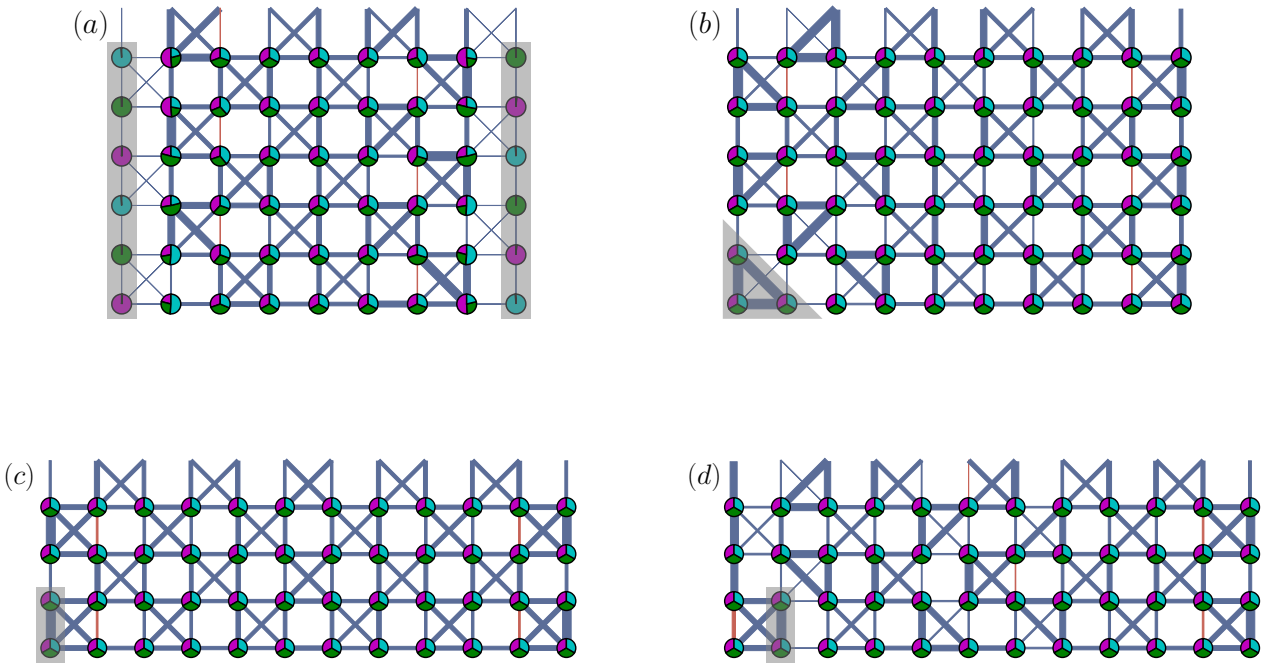

FIG. S1: Bond energies and local color densities on square lattice with different inducing structure on boundary (gray covered region). Open boundary condition on x direction and periodic boundary condition on y direction. (a) External fields inducing antiferromagnetic order applied on the boundary sites; (b) Stronger interaction on bonds in a triangle; (c) Stronger interaction on a single bond; (d) Stronger interaction on a single bond whose correlation is weak in previous results.

S2. DMRG SIMULATION OF DIFFERENT SIZES

Bond energies and local color densities are presented for different sizes of the system by DMRG calculations. We extend the $(7,4)$ system to $(10,4)$, which keeps the total number of spins a multiple of 3, and plot the real space patterns of the lowest

energy state and some competing states in FIG. S2

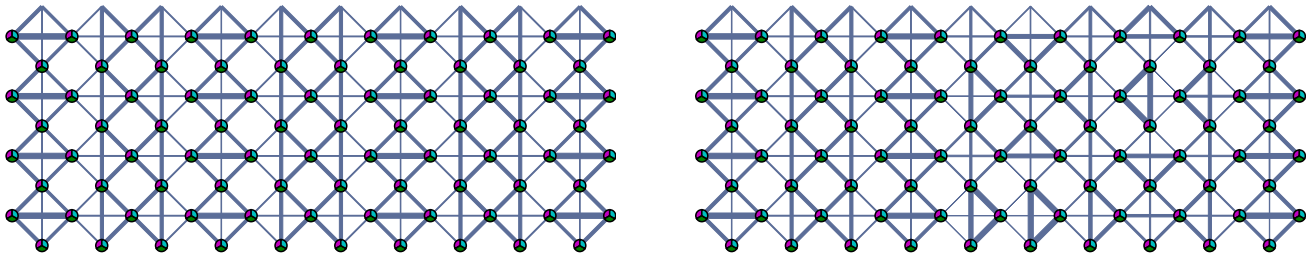

(a) $(10, 4)$ Stripe Structure

(b) $(10, 4)$ Local Minimum

FIG. S2: Ground state (S2a) and local minimum state (S2b) real-space bond strength obtained by DMRG simulation for the system size of $(10, 4)$. The energy of the states are (S2a) $E_0 = -286.548$, (S2b) $E_1 = -286.283$. Their pattern could be regarded as patterns of 7×4 low energy states with an extra stripe period.

Then we extend the size in y direction to $(7, 5)$ and $(7, 6)$. The results are shown in FIG. S3.

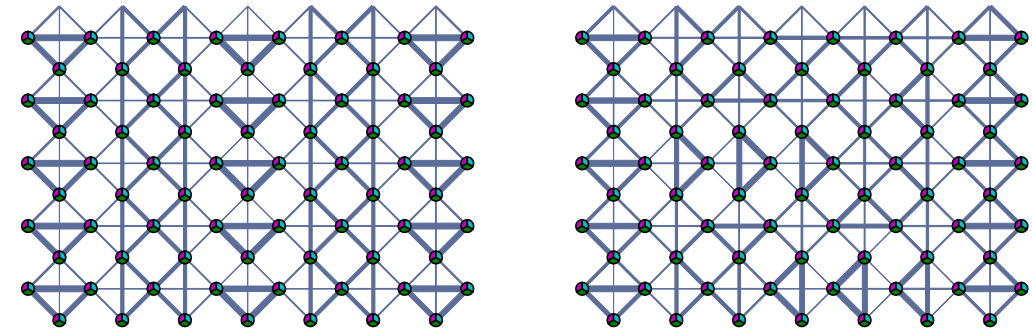

(a) $(7, 5)$ Stripe Structure

(b) $(7, 5)$ Local Minimum

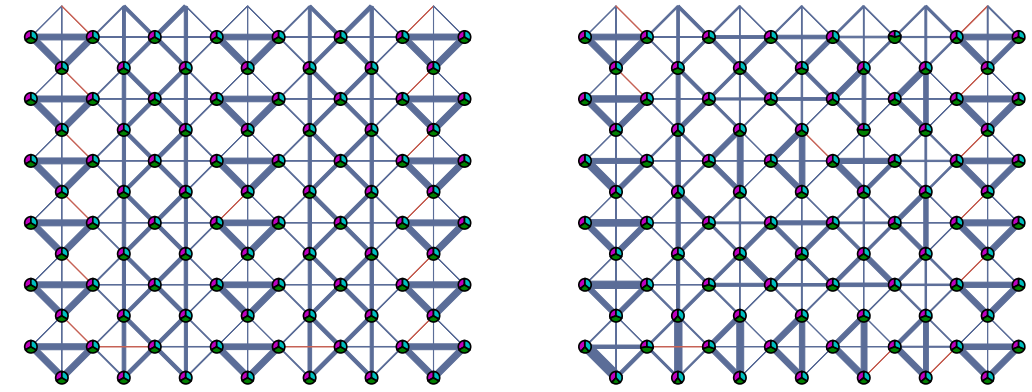

(c) $(7, 6)$ Stripe Structure

(d) $(7, 6)$ Local Minimum

FIG. S3: Ground state (S3a, S3c) and local minimum state (S3b, S3d) real-space bond strength obtained by DMRG simulation for the system size of $(7, 5)$ and $(7, 6)$. The energy of the states are (S3a) $E_0 = -250.928$, (S3b) $E_0 = -250.520$, (S3c) $E_0 = -300.598$, (S3d) $E_0 = -299.661$. The energy of bond stripe states are lower.

When the size in y direction is 6, we can freely set up the size in x direction with the total spin number a multiple of 3. The results are shown in FIG. S4.

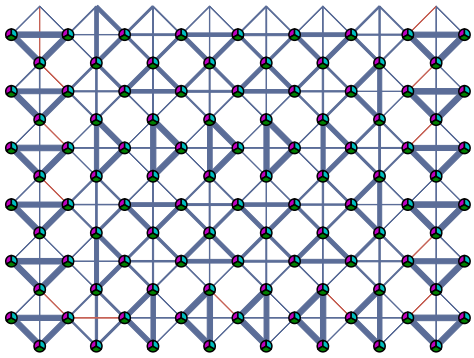

(a) $(8, 6)$ triangle pattern A

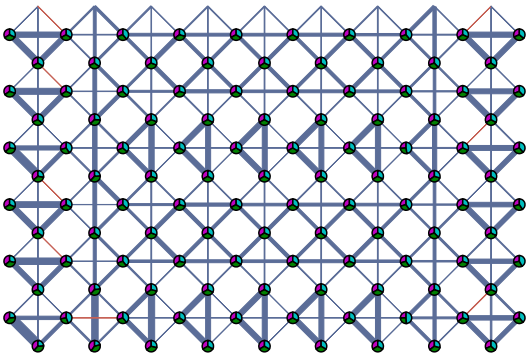

(b) $(9, 6)$ local minimum

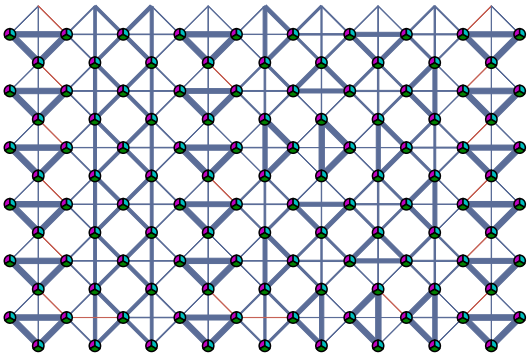

(c) $(9, 6)$ stripe with triangle pattern A

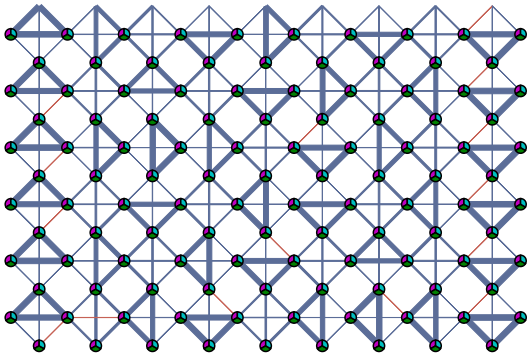

(d) $(9, 6)$ triangle pattern B

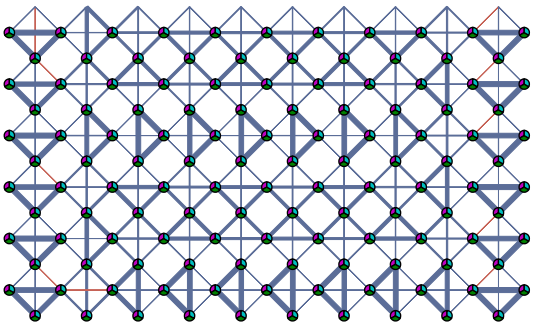

(e) $(10, 6)$ triangle pattern A

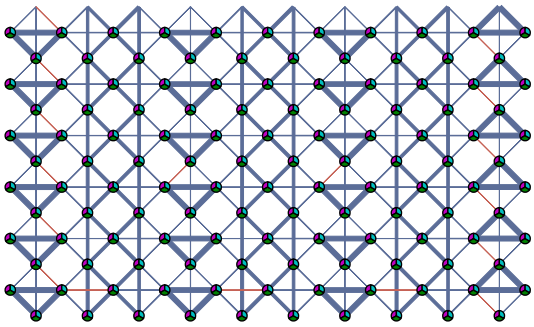

(f) $(10, 6)$ stripe pattern

FIG. S4: Ground states and local minimum states obtained by DMRG simulation for the system width $N_y = 6$. The energy of the states are (S4a) $E_0 = -342.361$, (S4b) $E_0 = -384.193$, (S4c) $E_0 = -384.550$, (S4d) $E_0 = -384.070$, (S4e) $E_0 = -426.819$, (S4f) $E_0 = -426.903$. The bond stripe states have better energy.

S3. LOW ENERGY EFFECTIVE THEORY OF LOCAL TRIANGLE SINGLET

The arrow mapping rule is shown in FIG. S5 and a real space example is shown in FIG. S6.

Through the mapping, we can see that the local triangle singlet in the low energy effective theory is mapped to a restricted vertex model space. This vertex model space has only sources and no sinks. The flow of arrows is not a constant, but it enters into a loop. In the previous finite size DMRG calculation, we can find that the boundary configurations are loop structures. As shown in FIG. S7, for the system size $(N_x, N_y) = (9, 6)$, there are two inner structures. They are both devided by a in-body loop structure.

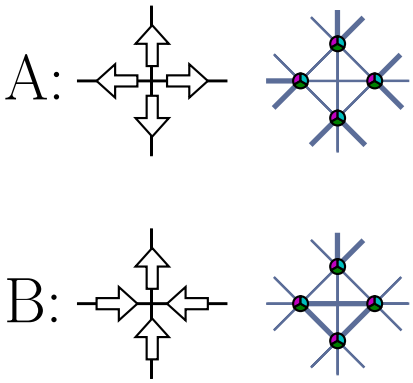

FIG. S5: Mapping for the local triangle singlet to the arrow representation: case A represents four spins in the unit cell form a 3-spin singlet in its surrounding unit cell; case B represents three spins in the unit cell form a SU (3) singlet, and one spin forms singlet in the adjacent unit cell.

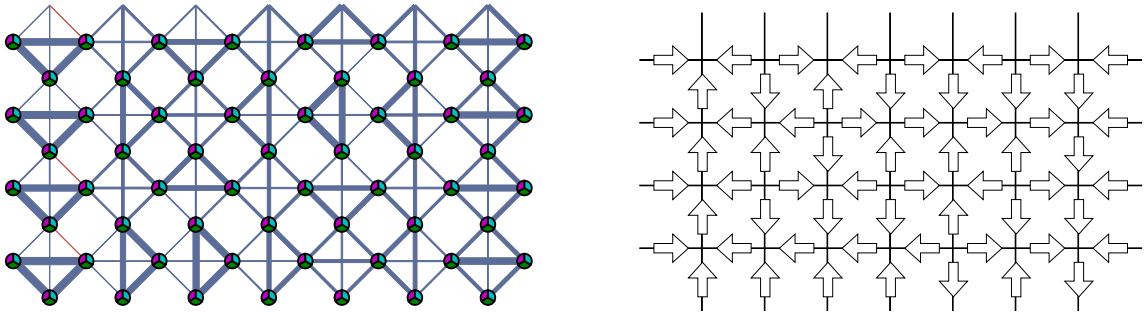

FIG. S6: An example of the local triangle singlet for the system size $(4, 7)$ and its arrow representation.

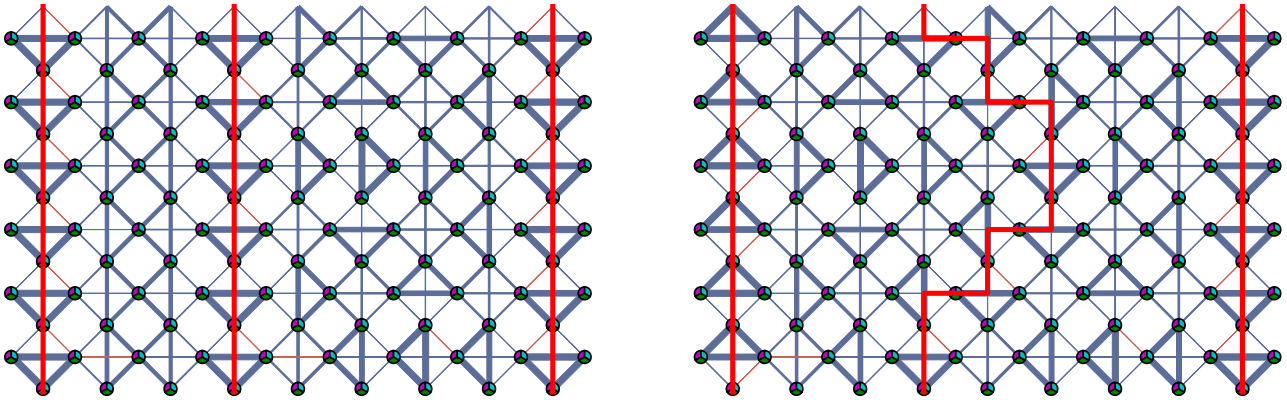

FIG. S7: Two loop structures for the system size $(N_x, N_y) = (9, 6)$, labeled by red lines. obviously, the reverse operation on the arrows also corresponds to a real space configuration.